Quantifying the pattern of organic carbon burial through Cretaceous Oceanic Anoxic Event 2

Huifang Guo[a,b], Xi Chen[a,c,*], Hanwei Yao[a,c], Yinggang Zhang[d,e], Benjamin J.W Mills[e], Kaibo Han[a,f], Shujuan Wu[a,c], Yida Yang[a,b], Zihao Wang[b], David B. Kemp[g]

a State Key Laboratory of Biogeology and Environmental Geology, China University of Geosciences, Beijing 100083, China

b School of Earth Sciences and Resources, China University of Geosciences, Beijing 100083, China

c Institute of Earth Sciences, China University of Geosciences, Beijing 100083, China

d Nanjing Institute of Geology and Palaeontology, Chinese Academy of Sciences, Nanjing, China

e School of Earth and Environment, University of Leeds, Leeds LS2 9JT, UK.

f School of Earth Sciences, Hebei GEO University, Shijiazhuang 050031, China

g State Key Laboratory of Biogeology and Environmental Geology and Hubei Key Laboratory for Critical Zone Evolution, School of Earth Sciences, China University of Geosciences, Wuhan 430074, China

*Corresponding authors: Xi Chen (xichen@cugb.edu.cn)

Abstract

The Cenomanian-Turonian Oceanic Anoxic Event 2 (OAE 2, ca. 94 Ma) is characterized by a marked positive carbon isotope excursion (CIE) recorded in global marine basins. This CIE results from a global-scale increase in organic matter burial, facilitated by high productivity and seawater deoxygenation. To date, however, the precise pattern of changes in the burial rate of organic matter through the event has

not been well constrained. In this work, we present a compilation of data from 42 globally distributed OAE 2 sites, as well as organic carbon isotope ($\delta^{13}C_{org}$), total organic carbon (TOC), and trace element concentration data from a new OAE 2 interval in southern Tibet, China. In southern Tibet, the absence of redox-sensitive trace element enrichment through OAE 2 indicates prevailing oxic conditions. Organic carbon (OC) mass accumulation rate (MAR) at this site decreased from the lower part of the CIE to the upper part, in contrast to an approximate doubling of organic carbon MAR in the upper part observed globally. This result, coupled with detailed analysis of the compilation, shows that redox was a key factor controlling organic burial rates during OAE 2, with OC MAR scaling positively with increasing deoxygenation. Leveraging a biogeochemical model to simulate these data suggets that 5-20% of the seafloor became anoxic during OAE 2, and that this deoxygenation was accompanied by 100% to 200% increase in global seawater P concentration. Our findings indicate that during OAE 2, elevated nutrient levels may have resulted from enhanced recycling from sediments under reducing conditions, sustaining intensified primary production and subsequent organic carbon export and burial.

Keywords: OAE 2; Cenomanian-Turonian; Tibet; oceanic anoxia; organic carbon burial

1. Introduction

The Cretaceous Period witnessed elevated atmospheric CO_2 concentrations and temperatures, coinciding with episodic accumulation of organic carbon-rich sediments,

known as oceanic anoxic events (OAEs; Schlanger and Jenkyns, 1976). OAEs marked prolonged and significant perturbations to the global carbon cycle (Schlanger et al., 1987; Takashima et al., 2006; Jenkyns, 2010; Herrle et al., 2015; Gambacorta et al., 2016; Owens et al., 2017), expressed by widespread deoxygenation across numerous ocean basins. OAEs are commonly distinguished stratigraphically by positive carbon isotope ($\delta^{13}C$) excursions (CIEs) related to globally enhanced burial of organic carbon enriched in ^{12}C (Kump, 1991; Jenkyns, 2010; Bryant et al., 2021). Oceanic Anoxic Event 2 (OAE 2), occurring around ~94 Ma, represents a peak of organic matter (OM) burial, and is associated with a CIE of approximately 2.5‰ in marine carbonates and up to 4‰ in marine OM (e.g., Jarvis et al., 2006; Tsandev and Slomp, 2009; Owens et al., 2018; Paez-Reyes et al., 2021; Papadomanolaki et al., 2022). The $\delta^{13}C$ profiles through OAE 2 in different basins share a similar basic pattern. Specifically, the $\delta^{13}C$ evolution can be divided into six distinct stages (Li et al., 2017), of which stages C3, C4 and C5 define the OAE 2 interval. In stages C1 and C6, the carbon isotope curve exhibits relative stability, representing pre- and post-event baseline values, respectively. Larger-scale and higher frequency $\delta^{13}C$ fluctuations characterize stage C2, with a relatively minor $\delta^{13}C$ negative shift sometimes observed. Stage C3 shows an initial rapid transition to higher $\delta^{13}C$ values ('build-up' phase), followed by a 'plateau' phase (stage C4) with relatively constant $\delta^{13}C$ values and finally a 'recovery' phase (stage C5), where $\delta^{13}C$ values return to near-pre-event values.

Different hypotheses have been proposed to elucidate the mechanisms of enhanced organic matter accumulation during OAE 2 (e.g., Jenkyns, 2010; Beil et al.,

2020). These include the role of nutrient enrichment via emissions from large igneous provinces (LIPs) (Turgeon and Creaser, 2008; Trabucho Alexandre et al., 2010; Du Vivier et al., 2015; Schröder-Adams et al., 2019), remobilization from terrestrial areas due to marine transgressions (Jenkyns, 1980; Haq, 2014), input from intensified terrestrial weathering (Monteiro et al., 2012; Poulton et al., 2015; Jenkyns et al., 2017), and the release of phosphorus from sediments under benthic anoxic conditions (Mort et al., 2008; Wallmann, 2010; Beil et al., 2020). Understanding the triggers and mechanisms behind organic carbon enrichment during OAE 2 has significantly advanced in recent years (e.g., Schröder-Adams et al., 2019; Londoño and Collins, 2022). At the same time, previous studies have provided a robust estimate of the total organic carbon sequestration throughout the entire OAE 2 period, amounting to approximately 70 Eg (1 Eg = 10^{18} g), which exceeds the current marine carbon burial flux by more than two-fold (Owens et al., 2018). However, the variations in the organic carbon mass accumulation rates (OC MARs) across different CIE stages remain poorly understood, and the dominant drivers governing short-term organic carbon burial during the event also remain elusive. A key challenge in unraveling the driving forces and dynamics of OAE 2 is the uncertainties regarding its duration and the distinct stages it encompasses (Beil et al., 2020). The total duration of the CIE associated with OAE 2 has been previously estimated to have ranged from ~430 kyr to ~930 kyr (Sageman et al., 2006; Meyers et al., 2012; Ma et al., 2014; Eldrett et al., 2015; Li et al., 2017; Charbonnier et al., 2018; Gangl et al., 2019). A recent high-precision estimate of 619 kyr has been established cyclostratigraphically from site

SH#1 in the USA (Jones et al., 2019). Discrepancies in previous timescale estimates are largely attributable to varied definitions of the onset and end of OAE 2. For example, some estimates are based on the stratigraphic pattern and magnitude of organic-enrichment, while others are based on the stratigraphic pattern of the CIE (Beil et al., 2020).

A robust understanding of OC MAR from globally distributed basins is a key prerequisite for understanding the precise pattern of global organic matter burial across OAE 2, and for interpreting the associated carbon isotope excursion. To date, however, only a few sites have been reported from the southern hemisphere and eastern Tethys Ocean. In this study, we have investigated the OC burial history and paleoenvironment during OAE 2 in the Qiangdong section, which was deposited on the southern margin of the eastern Tethys Ocean during the Cretaceous (Fig. 1 and S1). OAE 2 in this section has been identified by biostratigraphy (Jia et al., 2010) and low-resolution $\delta^{13}C_{org}$ curve (Zhang et al., 2016). We integrate these new data with previously published data from 42 globally distributed sites (Fig. 1) to assess the temporal pattern of OC MARs for different CIE stages at each site. Through this analysis, we establish a unified organic carbon burial rate curve for OAE 2, permitting precise comparison of OC MAR variations in a spatiotemporal context. In so doing, we investigate the drivers of short-term organic matter sequestration rates during OAE 2.

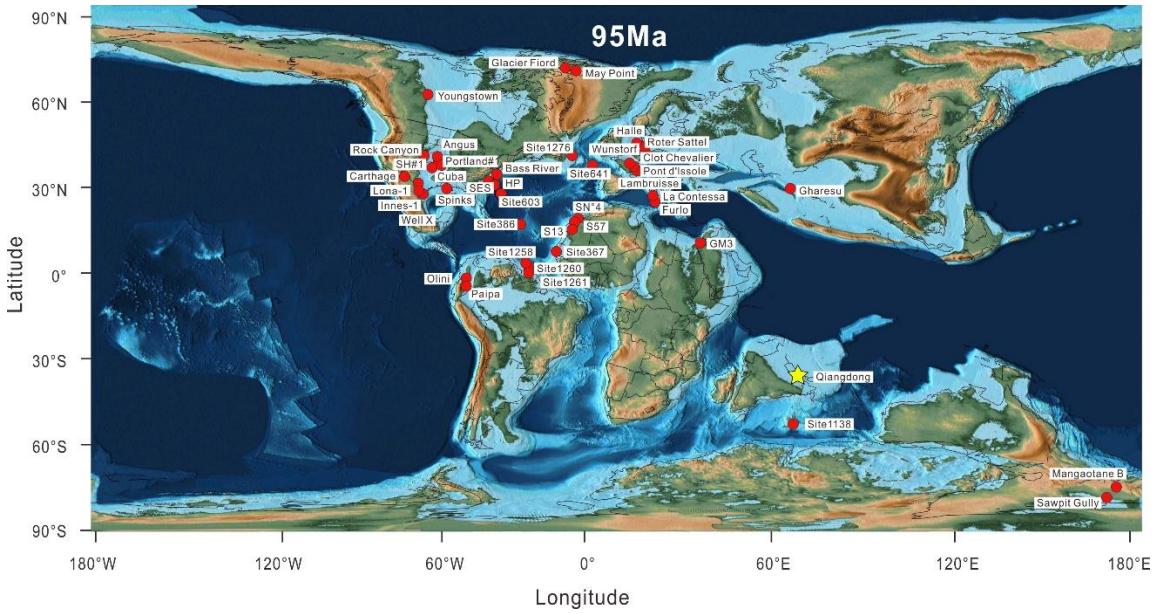

Fig. 1. Paleogeographic map (95 Ma, Cenomanian) and locations of OAE 2 sections (red dots). Referenced sources are detailed in Table 1. The yellow star marks the Qiangdong section. The map is adapted from the PALEOMAP Project (Scotese, 2016).

2. Materials and Methods

2.1 Sample preparation and analysis in the Qiangdong section

In total, 72 samples with a spacing of 1 m were taken from the OAE interval (~72 m thick) of the Qiangdong section for organic carbon isotope and TOC analysis, and 37 samples with a spacing of 2 m were selected for major and trace element analyses. To prevent sampling of oxidized or contaminated material, weathered surfaces and visibly altered parts were trimmed off before grinding into a fine powder. The residual rock samples were crushed and ground to 200 mesh powder for subsequent analysis. Methods used for the measurement of organic carbon isotopes, TOC, and major and trace element abundance are described in detail in the Supplementary Materials.

2.2 Data compilation and measurement of mass-accumulation rates

OAE 2 is one of the most widely documented carbon cycle perturbation events in the geological record (e.g., Bowman and Bralower, 2005; Jenkyns, 2010; Eldrett et al., 2017; Beil et al., 2018; Jones et al., 2021; Paez-Reyes et al., 2021; McDonald et al., 2022). We compiled data from 43 globally distributed OAE 2 sections that each clearly show the OAE 2 CIE, including the Qiangdong section (Fig. 1). Unlike the compilation approach of Owens et al. (2018), the selected sections only include those dominated by black shale facies, rather than carbonates, as previous studies have shown that carbonates typically have low TOC content. Following Kemp et al. (2022), we classify the redox state of each section, as reported in the literature, into three types: oxic-suboxic, suboxic-anoxic, and anoxic-euxinic. Detailed information on the compiled sections is provided in Table 1, with comprehensive information on the redox of each site provided in the Supplementary Materials Table S1.

The organic carbon burial rate during OAE 2 can be quantified for each of our studied sections using the available TOC data coupled with knowledge of rock density and bulk sediment accumulation rates. Hence, organic carbon mass accumulation rate (MAR; $g/cm^2/kyr$) is calculated by:

$$MAR[g/cm^2/kyr] = LSR\ [cm/kyr] \times \rho\ [g/cm^3] \times TOC\ [wt\%]$$

where LSR is the linear sedimentation rate, and ρ is rock density. Few rock density data have been previously published, and we assume instead (following Owens et al., 2018) a constant density of 2.4 g/cm^3, which is lower than the typical mudstone density of ~2.7 g/cm^3 since organic-rich rocks have generally lower density. In any case, the exact density value chosen has only a limited effect on the absolute

MAR values calculated, and has no effect on calculations of changes in organic carbon burial rate.

The linear sedimentation rates for each section are calculated by using the reported CIE stratigraphic thickness and the estimated duration of the CIE interval. As noted in Section 1, this duration of OAE 2 has been previously estimated using different methods (Sageman et al., 2006; Meyers et al., 2012; Ma et al., 2014; Eldrett et al., 2015; Li et al., 2017; Charbonnier et al., 2018; Gangl et al., 2019; Jones et al., 2019). In this study, we use the published timescales for each section, if available. If the duration was not previously published, we adopt a duration of 619 kyr, based on the astronomically tuned OAE 2 duration obtained recently from site SH#1, USA (Jones et al., 2019). Importantly, this timescale provides estimated durations for the different stages of the CIE: 193 kyr for stage C3, 324 kyr for stage C4 and 102 kyr for stage C5 (Jones et al., 2019). The stratigraphic thickness of the OAE 2 interval and individual stages in each section was defined by the available organic carbon isotope data and assumes unchanging sedimentation rate and no major stratigraphic gaps.

Table 1. The list of sites studied in this study, including data on stratigraphic thickness, organic carbon burial rates, and inferred redox, along with references. Question marks denote uncertain redox interpretation. The locations of the sites are shown in Fig. 1. WIS: Western Interior Seaway.

Site No.	Area	Study site	Thickness (m)	OC MAR ($g/cm^2/kyr$)	Redox interpretation	Reference (duration from)	Reference (data from)
1	USA (WIS)	Carthage	22.00	0.05	Suboxic-anoxic	Jones et al. (2019)	Bryant et al. (2021)
2	USA (WIS)	Iona-1 Core	18.03	0.11	Anoxic-euxinic	Eldrett et al. (2017)	Eldrett et al. (2015)
3	USA (WIS)	SH#1 Core	17.47	0.07	Anoxic-euxinic	Jones et al. (2019)	Jones et al. (2019)
4	USA (WIS)	Portland#1	7.99	0.03	Suboxic-anoxic	Eldrett et al. (2017)	McDonald et al. (2022)
5	USA (WIS)	Angus Core	11.39	0.09	Anoxic-euxinic	Jones et al. (2021)	Jones et al. (2021)
6	USA (WIS)	Cuba, Kansas	3.27	0.05	Suboxic-anoxic	Jones et al. (2019)	Bowmana et al. (2005)

7	USA (WIS)	Rock Canyon	7.00	0.02	Anoxic-euxinic	Jones et al. (2019)	Bowmana et al. (2005)
8	USA (WIS)	Innes-1 Core	12.04	0.06	Anoxic-euxinic	Eldrett et al. (2017)	Eldrett et al. (2017)
9	USA (WIS)	Well “X” core	17.65	0.09	Suboxic-anoxic	Eldrett et al. (2017)	Eldrett et al. (2017)
10	Canada (WIS)	Youngstown	14.40	0.36	Anoxic-euxinic?	Jones et al. (2019)	Prokoph et al. (2001)
11	High Canadian Arctic	May Point	12.00	0.22	Anoxic-euxinic	Jones et al. (2019)	Lenniger et al. (2014)
12	High Canadian Arctic	Glacier Fiord	21.40	0.44	Suboxic-anoxic	Jones et al. (2019)	Schröder-Adams et al. (2019)
13	Gulf of Mexico	Spinks Core	14.87	0.11	Suboxic-anoxic	Jones et al. (2019)	Lowery et al. (2017)
14	USA (North Atlantic)	HP core	19.42	0.04	Suboxic-anoxic	Jones et al. (2019)	Lowery et al. (2021)
15	USA (North Atlantic)	SES core	10.82	0.04	Anoxic-euxinic?	Jones et al. (2019)	Lowery et al. (2021)
16	USA (North Atlantic)	Bass River	14.65	0.06	Oxic-suboxic	Jones et al. (2019)	van Helmond et al. (2014a)
17	Colombia (North Atlantic)	Paipa	11.90	0.27	Suboxic-anoxic	Paez-Reyes et al. (2021)	Paez-Reyes et al. (2021)
18	Colombia (North Atlantic)	Olini	6.05	0.12	Suboxic-anoxic	Paez-Reyes et al. (2021)	Paez-Reyes et al. (2021)
19	Demerara Rise (North Atlantic)	ODP Site 1260	1.60	0.03	Anoxic-euxinic	Eldrett et al. (2017)	Forster et al. (2007)
20	Demerara Rise (North Atlantic)	ODP Site 1258	4.68	0.27	Anoxic-euxinic	Jones et al. (2019)	Erbacher et al. (2005)
21	Demerara Rise (North Atlantic)	ODP Site 1261	9.13	0.26	Anoxic-euxinic	Eldrett et al. (2017)	Erbacher et al. (2005)
22	Morocco (North Atlantic)	S57	17.72	0.59	Anoxic-euxinic	Jones et al. (2019)	Tsikos et al. (2004)
23	Morocco (North Atlantic)	SN°4	41.94	1.30	Anoxic-euxinic	Beil et al. (2018)	Beil et al. (2018)
24	Morocco (North Atlantic)	S13	44.57	1.90	Anoxic-euxinic	Jones et al. (2019)	Kuypers et al. (2002)
25	North Atlantic	DSDP Site 367	5.60	0.94	Anoxic-euxinic	Jones et al. (2019)	Dickson et al. (2016)
26	North Atlantic	DSDP Site 386	6.38	0.18	Anoxic-euxinic	Jones et al. (2019)	van Helmond et al. (2014b)
27	North Atlantic	DSDP Site 603	5.03	0.10	Anoxic-euxinic	Jones et al. (2019)	van Helmond et al. (2014b)
28	North Atlantic	DSDP Site 641	1.09	0.01	Anoxic-euxinic	Jones et al. (2019)	van Helmond et al. (2014b)
29	North Atlantic	ODP Site 1276	3.97	0.05	Suboxic-anoxic	Jones et al. (2019)	Westermann et al. (2014)
30	France (Western Tethys)	Pont d'lssole	15.85	0.04	Suboxic-anoxic	Jones et al. (2019)	Jarvis et al. (2011)
31	France (Western Tethys)	Lambruisse	15.20	0.05	Suboxic-anoxic	Jones et al. (2019)	Danzelle et al. (2020)
32	France (Western Tethys)	Clot Chevalier	19.85	0.08	Suboxic-anoxic	Jones et al. (2019)	Gale et al. (2019)
33	Germany (Western Tethys)	Wunstorf	14.38	0.03	Suboxic-anoxic	Jones et al. (2019)	Du Vivier et al. (2014)
34	Germany (Western Tethys)	Halle	9.37	0.02	Anoxic-euxinic?	Jones et al. (2019)	Voigt et al. (2007)
35	Italy	La Contessa	0.72	0.02	Anoxic-	Jones et al. (2019)	Westermann

	(Western Tethys)				euxinic		et al. (2014)
36	Italy (Western Tethys)	Furlo	1.04	0.03	Anoxic-euxinic	Jones et al. (2019)	Westermann et al. (2014)
37	Jordan (Western Tethys)	GM3 CTB	15.14	0.04	Suboxic-anoxic	Jones et al. (2019)	Sepúlveda et al. (2009)
38	Switzerland (Western Tethys)	Roter Sattel	3.52	0.02	Anoxic-euxinic	Charbonnier et al. (2018)	Charbonnier et al. (2018)
39	Pacific Ocean	Sawpit Gully	33.44	0.02	Oxic-suboxic	Gangl et al. (2019)	Gangl et al. (2019)
40	Pacific Ocean	Mangaotane B	10.92	0.01	Oxic-suboxic	Gangl et al. (2019)	Gangl et al. (2019)
41	Indian Ocean	ODP Site 1138	2.22	0.04	Anoxic-euxinic	Jones et al. (2019)	Dickson et al. (2017)
42	Iran (Eastern Tethys)	Gharesu	33.50	0.06	Oxic-suboxic	Jones et al. (2019)	Kalanat et al. (2018)
43	China (Eastern Tethys)	Qiangdong	23.00	0.03	Oxic-suboxic	Jones et al. (2019)	This study

2.3 Earth System Modeling

The Spatial Continuous Integration (SCION) model was used to explore potential mechanisms for organic matter burial and their links to climatic and environmental changes during OAE 2. SCION is a global biogeochemical model that integrates 3D spatial climate information from FOAM (Fast Ocean-Atmosphere Model; Goddéris et al., 2014) with the biogeochemical processes outlined in COPSE (Carbon-Oxygen-Phosphorus-Sulphur-Evolution) to predict the evolution of seawater chemistry over the entire Phanerozoic (Mills et al., 2021; Zhang et al., 2023). Validations of the model and detailed model descriptions are provided in Mills et al. (2021) and Zhang et al. (2023). The full model code and derivation are available at https://github.com.bjwmills/SCION.

With external forcings (e.g. degassing rate) fixed at 95 Ma, the SCION model inform a steady-state preceding OAE 2. With this steady-state, the riverine input of the key limiting nutrient phosphorus **(**P) is artificially set to increase by scaled with a time-dependent factor during the OAE 2 interval. This single forcing drives

fluctuations in the seawater P reservoir and additional organic cabron burial. The artificially altering P input fluxes in the model are not as realistic as employing fully dynamic modeling, however, they can help focus our understanding of the likely phosphorus cycling involved during OAE 2 and relationships between this, the organic carbon burial record, and the responses of redox changes in the water column. Except for these revisions in the SCION model, carbon isotope fractionation factor for photosynthesis is fixed at −27‰. This factor, within the range of −25‰ to −35‰ used previously in the model (Mills et al., 2021), was obtained from comparisons between our analyzed organic C isotope composition and previously reported inorganic C isotope composition.

3. Results

3.1 Paleoenvironment and OC MAR variations across OAE 2 in the Qiangdong section

3.1.1 Organic carbon isotopes

Bulk organic carbon isotopes ($\delta^{13}C_{org}$) of the Qiangdong section range from −26.50‰ to −24.27‰ (Fig. 2), which is consistent with previous studies in this area (Jia et al., 2010; Zhang et al., 2016). A large positive $\delta^{13}C_{org}$ excursion between 20m and 42m is identified as OAE 2 based on the regional and global comparable variations in lithology, $\delta^{13}C$, and foraminiferal biostratigraphy (Wang et al., 2001; Wan et al., 2003; Jarvis et al., 2006; Li et al., 2006; Zhang et al., 2016).

In our study, the use of high-resolution sampling allows more precise

identification of the different carbon isotope stages (C1-C6) compared to previous work (Zhang et al., 2016). At the base of the Qiangdong section, a segment with relatively stable $\delta^{13}C_{org}$ values is apparent (stage C1, ~0–17 m), with values varying between −25.51‰ to −24.94‰ (mean −25.16‰). Stage C2 (17–20m) is marked by a small-scale negative $\delta^{13}C_{org}$ excursion (~0.27‰), which was not previously recognised in this section (Zhang et al., 2016). Subsequently, $\delta^{13}C_{org}$ increases gradually from −25.14‰ to −24.27‰ (stage C3, 20–26m), interrupted by a brief negative shift (Fig. 2). The end of stage C3 is at ~26 m, where $\delta^{13}C_{org}$ reached a maximum value (−24.27‰). Within the subsequent plateau phase (stage C4, 26–38m), $\delta^{13}C_{org}$ values are around −24.80‰ with several small peaks and troughs <0.5‰ in magnitude. Thereafter, the recovery phase (stage C5, 38–42m) encompasses a marked decrease in $\delta^{13}C_{org}$ to a stable value of −25.12‰. The end of this stage marks the termination of the CIE. Above this, $\delta^{13}C_{org}$ is broadly stable (stage C6), through decreases again at around 57 m height (Fig. 2).

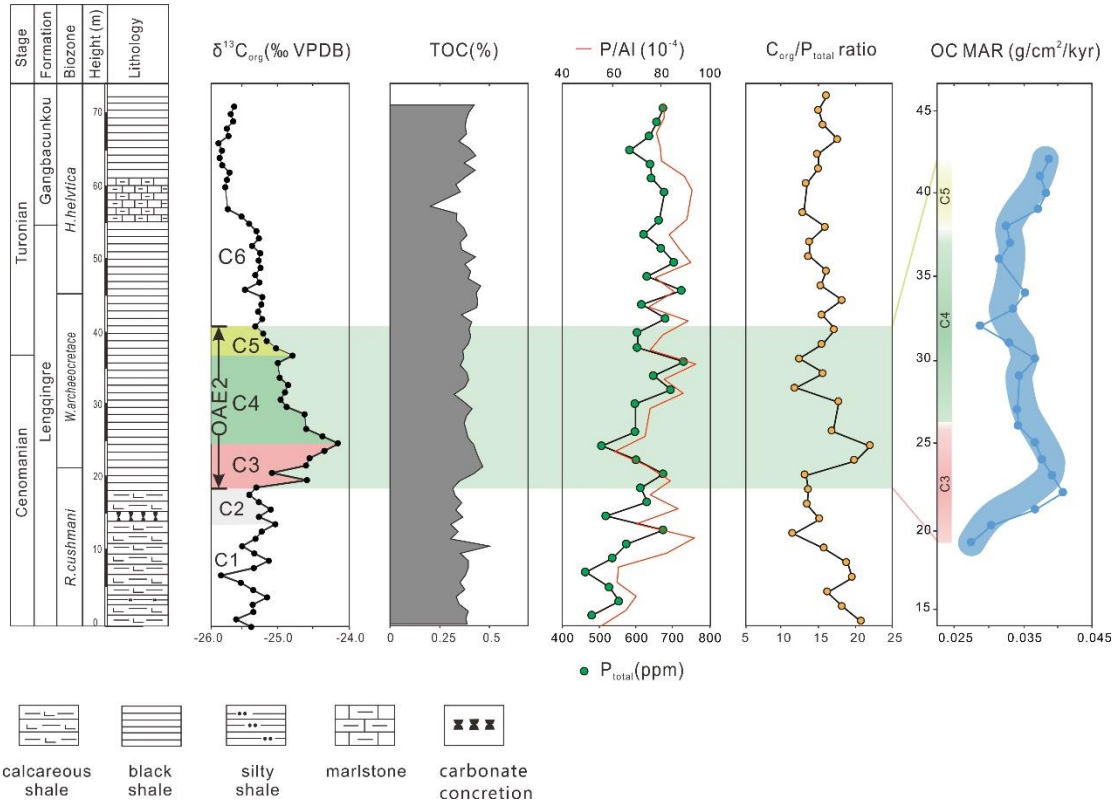

Fig. 2. Stratigraphic succession, carbon isotope composition, TOC content, Phosphorus contents, P/Al, atomic C_{org}:P_{tot} ratios and organic carbon burial rate (OC MAR) through the Qiangdong section. The light green shaded area represents the OAE 2 interval. The subdivisions of OAE 2 (stages C1-C6) are from Li et al. (2017). Blue bands show trends based on three-point average of the OC MAR data.

3.1.2 TOC and OC MAR variation

The total organic carbon (TOC) content of the Qiangdong section varies between 0.20 wt% and 0.50 wt% (Fig. 2). The most distinctive feature of the TOC profile is that the values fluctuate between 0.30 wt% and 0.45 wt% for the majority of the record, and is broadly stable except for some minor and transient positive and negative shifts.

The pre-OAE 2 interval (C1 and C2) generally exhibits low TOC content (<0.40 wt%), except for a single sample at 11 m with a value of 0.50 wt%. At the base of

stage C3, TOC content increases slightly and is followed by an interval of relatively constant TOC of ~0.4 wt‰ throughout the stage C3. However, the OC MARs increase rapidly to 0.04 (g/cm^2/kyr) in the lower part of stage C3 and then decrease gradually in the upper part of this stage (Fig. 2). TOC values of ~0.4 wt‰ persist throughout the remainder of the section and are interrupted by a small decrease at ~57 m. In stage C4, OC MARs maintain low levels, with minor fluctuations around 0.03 g/cm^2/kyr (except for a low value), followed by a small increase during stage C5 (Fig. 2).

3.1.3 Phosphorus content and C_{org}: P_{tot} ratios

Total phosphorus (P_{tot}) concentrations in the Qiangdong section vary between 450 ppm and 750 ppm (Fig. 2). When normalized against Al, the trend in P_{tot}/Al correlates very well with the P_{tot} variations, strongly suggesting that P_{tot} variations are independent of lithological changes. The pre-OAE 2 interval (stages C1 and C2) is characterized by relatively variable but progressively increasing P_{tot} and P_{tot}/Al. Above this, P_{tot} decreases to 509 ppm through stage C3 and the start of stage C4 in the OAE 2 interval, and there is also a corresponding minima reached in P_{tot}/Al. P_{tot} and P_{tot}/Al increase again through most of stage C4. P_{tot} and P_{tot}/Al values in stage C5 and above the CIE to the top of the studied succession are broadly stable. As such, P content does not show any clear change at the termination of OAE 2.

C_{org}/P_{tot} ratios have been proposed as a reliable indicator of seafloor redox conditions in marine environments (Algeo and Ingall, 2007; Mort et al., 2008; Kraal

et al., 2010; Beil et al., 2020). The C_{org}/P_{tot} ratio in the Qiangdong section mirrors the trend in P_{tot} (Fig. 2). C_{org}/P_{tot} in the strata below OAE 2 show a stepwise decreasing trend. Stage C3 is characterized by a sharp increase from ~13 to ~22. C_{org}/P_{tot} then gradually decreases to a minimum of ~12 during stage C4 and increases slightly during stage C5. Above stage C5, C_{org}/P_{tot} returns to relatively stable background values, with an average of 15.3.

3.1.4 Trace element record

The enrichment or depletion of redox-sensitive trace elements (RSTEs) in sediments depends on the availability of oxidants, making them useful indicators for deciphering the paleo-redox conditions related to organic-rich sediments (Brumsack, 2006; Tribovillard et al., 2006; Turgeon and Brumsack, 2006). Mo, V and U are generally show enrichment under O_2-depleted conditions. In addition, these elements have minimal terrigenous sources, and are thus considered as robust proxies for the assessment of seawater redox conditions (Tribovillard et al., 2006; Algeo and Tribovillard, 2009). Cu, Ni and Ba are micronutrients and are consequently widely employed as palaeoproductivity indicators. Raw and Al-normalized RSTE data from the Qiangdong section are shown in Fig. 3.

The concentrations of Mo are exceptionally low in the Qiangdong section, with almost all the data falling close to the detection limit of our analysis (~0.5 ppm). These Mo/Al values are well below that of average shale. U concentrations are also low, with all U/Al values below those of average shale. In contrast to Mo and U, V/Al values are higher than average shale and values are stable through the studied

succession.

No enrichments of Cu and Ba are observed across the section, with all Al-normalized values remaining broadly stable and significantly below average shale values. Ni/Al values are close to those of average shale.

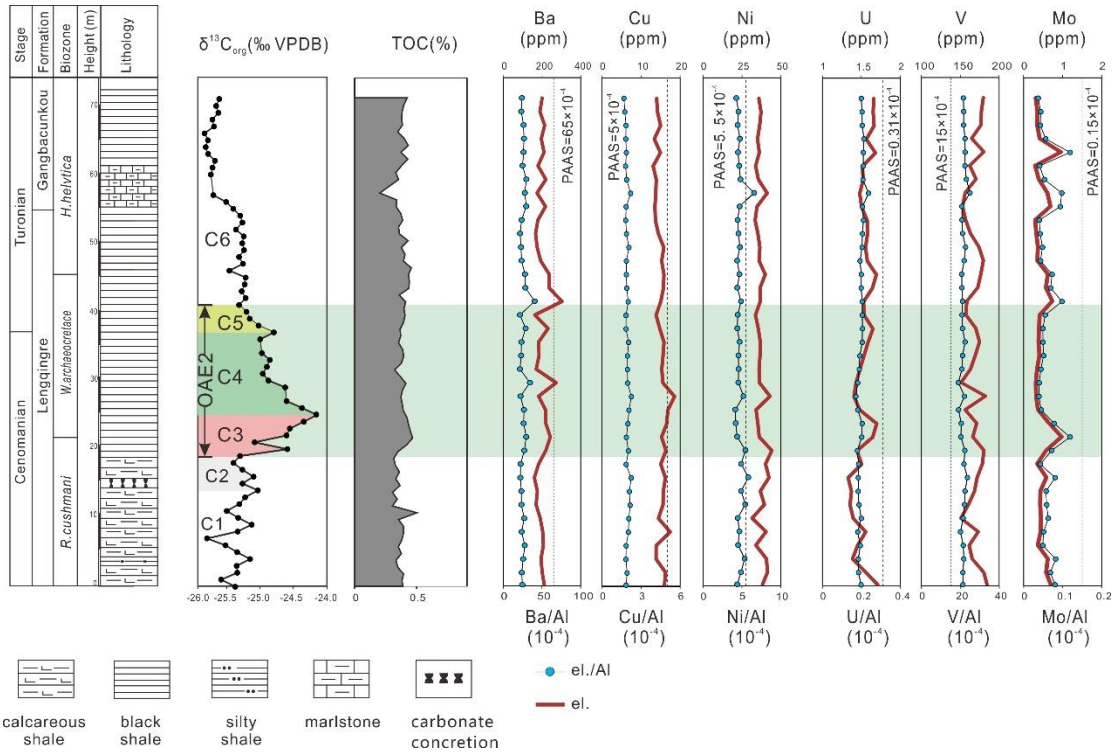

Fig. 3. Evolution of the redox-sensitive trace elements (RSTEs) (Mo, V, U), and elements associated with primary productivity (Ba, Cu, Ni) throughout the Qiangdong section. The red curves represent element concentrations, and the blue dots represent elements normalized to Al. The Al-normalized average shale values (post-Archean Australian shale, PAAS, dashed lines) are taken from Taylor and McLennan (1985).

3.2 Global record of OC MARs during OAE 2

Our compilation of 43 global sections (including Qiangdong) comprises sections that have been extensively studied in biostratigraphy and carbon isotopic stratigraphy (Fig. 1). As such, the stratigraphic framework of the sections is well constrained, with

well-defined C/T boundaries and biostratigraphic zonation schemes. Ages obtained through astronomical tuning of the OAE 2 interval thus allow high-resolution calculation of the OC MARs for the different substages. The average OC MAR values determined for each site span from 0.01 to 1.9 g/cm^2/kyr during OAE 2 (Fig. 4). Regions of inferred upwelling (e.g., Morocco) exhibit the highest values. Among the 43 sections, 39 localities have average OC MAR values less than 0.5 g/cm^2/kyr (including Qiangdong). Specifically, the majority of sites located in the WIS have organic carbon burial rates between 0.05 and 0.1 g/cm^2/kyr, while most sites in Tethys exhibit organic carbon burial rates below 0.05 g/cm^2/kyr.

Based on the compiled data from the 43 sites, we also generated a curve of mean OC MAR values in each stage of OAE 2 by employing bootstrap resampling (20,000 times) to ascertain the average value for each stage along with the 1-sigma standard deviation (Fig. 5). The bootstrap method mitigates the risk of over-reliance on individual data points (Singh and Xie, 2008). A mean value of 0.05 g/cm^2/kyr, as determined in previous studies, was regarded as the background value for stages C1-2 and C6 (Owens et al., 2018). The results show that the OC MAR during stage C3 (0.109 g/cm^2/kyr) is twice that of the background value. In stage C4, this rate (0.224 g/cm^2/kyr) increases to four times the background level. Notably, the burial rate in stage C5 (0.215 g/cm^2/kyr) is comparable to that observed in stage C4 (Fig. 5; Table 2). Unlike most sites, however, in our Qiangdong section OC MAR during stage C3 is slightly higher than in stage C4 (Fig. 2). Here, the accumulation rates of organic carbon increase in the lower part of stage C3, reaching a maximum value of ~0.04

g/cm^2/kyr. Thereafter, the accumulation rates gradually decrease to relatively low values that persist throughout stage C4. Stage C5 shows a slight increase in OC MARs.

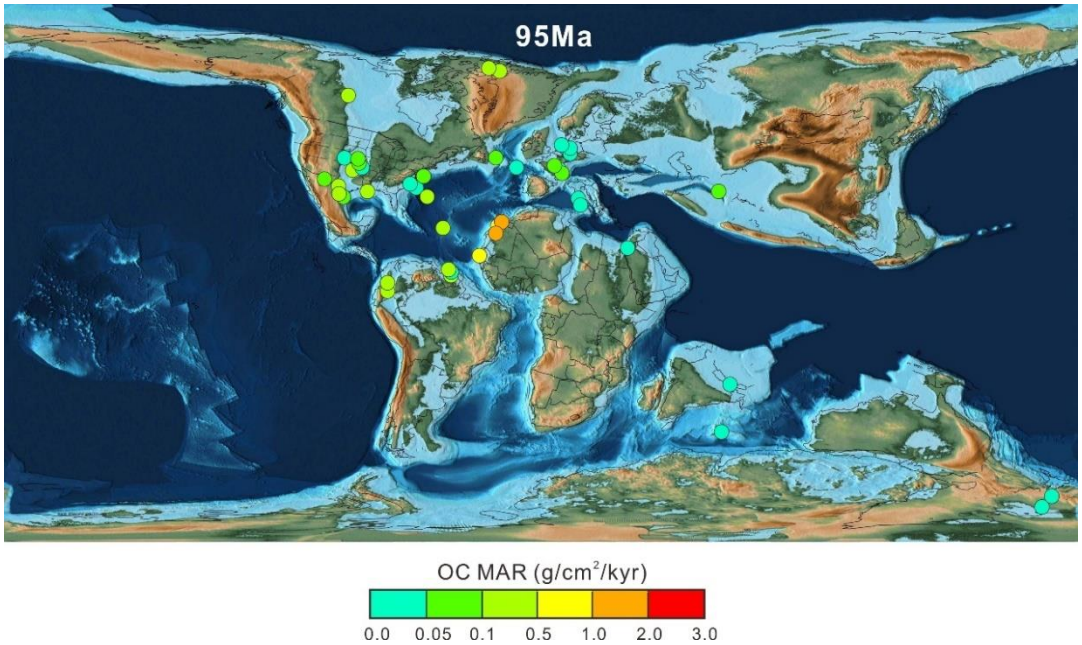

Fig. 4. Global pattern of calculated OC MAR for each site. Each coloured data point denotes data from a specific location with available high-resolution carbon isotope and TOC data (see also Table 1). The map is adapted from the PALEOMAP Project (Scotese, 2016).

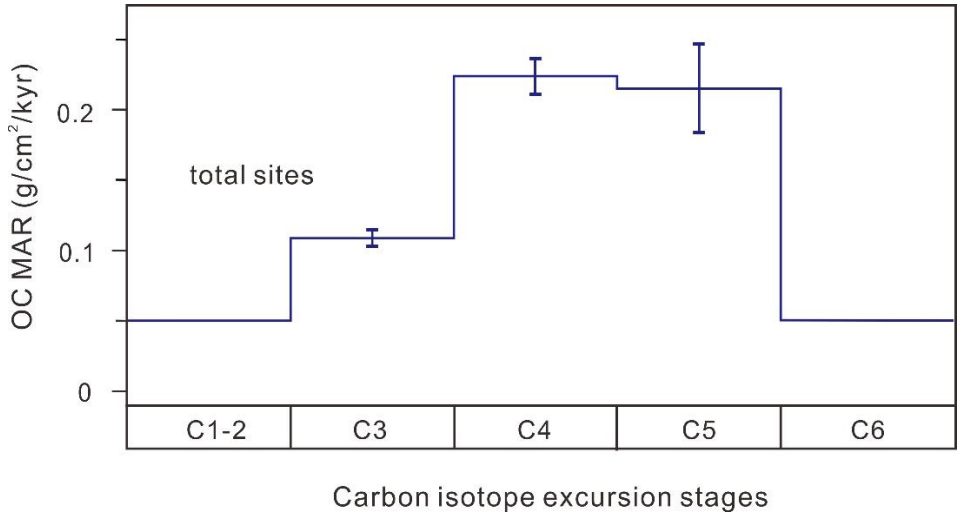

Fig. 5. Composite average value curve of all organic carbon burial rates (OC MARs) data for each

stage of the OAE 2 CIE (stages C3-C5, with 1σ error bars) obtained by bootstrap resampling method, based on global compilation of all 43 sections. Stages C1-2 and C6 represent the pre- and post-event intervals, respectively, with OC MAR set to 0.05 g/cm^2/kyr in these intervals (see main text). Detailed data are shown in Table 2.

4. Controls on organic enrichment during OAE 2

4.1 The role of seawater redox

Organic matter accumulation in marine environments is governed by the interplay of primary productivity, preservation conditions and dilution (e.g., Tessin et al., 2015; Lowery et al., 2021; Wang et al., 2021). Numerous studies have documented a covariance between redox sensitive trace elements (RSTEs, e.g., Mo, U, V) and TOC concentrations in ancient sediments and rocks (e.g., Algeo and Maynard, 2004; Tribovillard et al., 2006), thus supporting a link between redox conditions and organic carbon burial/preservation. In the Qiangdong section, there are no significant enrichments of TOC or RSTEs through the studied interval (Fig. 3; Fig. 6), indicating oxic conditions during OAE 2 on the shelf of East Tethys.

Redox conditions of the compiled sites during OAE 2 varied from oxic to euxinic (Table 1, see also Section 2.2). During OAE 2, the seafloor of the proto-North Atlantic Ocean was mainly anoxic-euxinic. In contrast, the seafloor of the Eastern Tethys and Pacific Oceans appear to have been dominantly oxic. The Western Interior Seaway (WIS) and Western Tethys were mainly suboxic-anoxic (Table 1).

The recorded redox states of different sites is typically evidenced by geochemical proxies, including Mo and U enrichments (Algeo and Maynard, 2004; Algeo and

Tribovillard, 2009). In Fig. 6, we compiled available Mo-U data (quantified as enrichment factors) across OAE 2 from global basins (Fig. 6). The data emphasize the well-oxygenated condition in Qiangdong, the generally suboxic to anoxic conditions in the WIS (Portland-1 and Well "X" cores), the more severe reducing conditions (close to the anoxic/euxinic threshold) in the Iona-1 and Innes-1 cores, and the fully euxinic conditions in the Cape Verde Basin (ODP Site 367) and at Demerara Rise (ODP Site 1261).

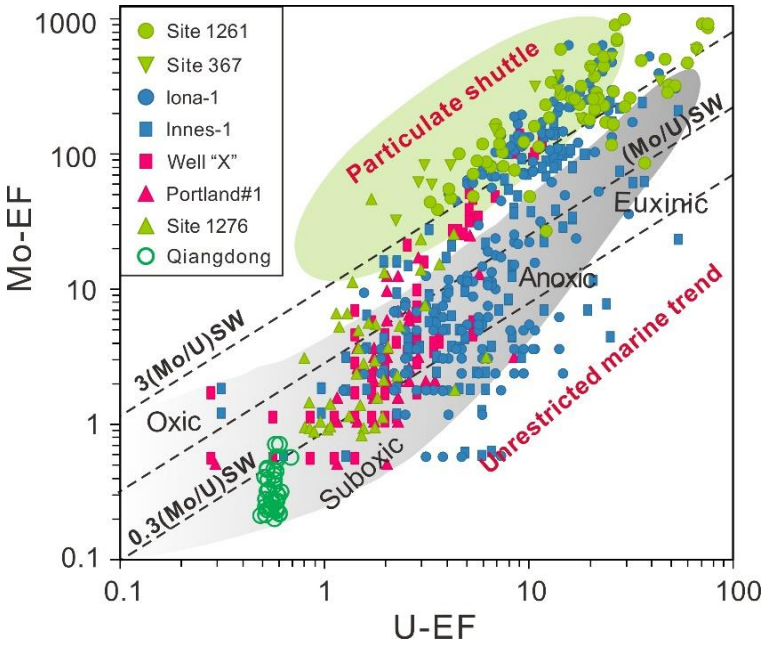

Fig. 6. Mo-EF (enrichment factor) versus U-EF for the Qiangdong section (this study), ODP Site 1261 and DSDP Site 367, Iona-1, Innes-1, Well "X", Portland#1 and Site1276. EF was calculated as $EF(X) = (X / Al)_{sample} / (X / Al)_{PAAS}$ (PAAS: post-Archean Australian shale, from Taylor and McLennan, 1985). Data sources are listed in Table 1. Diagonal dashed lines indicate the 3/1, 1/1 and 0.3/1 (Mo/U) ratios of present-day seawater. The area of gradient grey maps the Mo-EF vs. U-EF evolution under suboxic to euxinic conditions in modern unrestricted marine environments, as observed in eastern tropical Pacific sites (Tribovillard et al., 2012). The green area represents the "Particulate Shuttle" effect values, characteristic of weakly restricted basins (Tribovillard et al., 2012).

366 We also used the method of bootstrap resampling (see Section 3.2) to create
367 separate composite OC MAR curves across OAE 2 for sites with different redox
368 states (Fig. 7). These data are presented in Table 2. The results show that OC MAR
369 values are strongly dictated by the redox conditions at the studied sites (Fig. 7). The
370 highest organic matter burial rates predominantly occur at anoxic-euxinic sites, with
371 an average OC MAR of 0.27 g/cm^2/kyr during OAE 2. In contrast, oxic-suboxic areas
372 have the lowest OC MAR, averaging at 0.04 g/cm^2/kyr. Suboxic-anoxic sites have an
373 average OC MAR of 0.1 g/cm^2/kyr, relatively close to that of oxic-suboxic sites (Fig.
374 7). Numerous previous studies have also shown that there is a clear correlation
375 between redox-sensitive elements (e.g., Mn, V/Cr) and organic carbon burial rate (e.g.,
376 ODP Site 1276, Westermann et al., 2014). This relationship underscores the influence
377 of redox on organic carbon sequestration in marine sedimentary environments (e.g.,
378 Danzelle et al., 2018; Wang et al., 2021).
379 Redox state also played a key role in determining the changing magnitude in OC
380 MAR through OAE 2 (Fig. 7). OC MAR values show the most substantial changes at
381 anoxic-euxinic sites. Indeed, OC MAR in oxic-suboxic areas did not significantly
382 change through OAE 2, and only a modest increase occurred at suboxic-anoxic sites.
383 In order to describe the change of OC MARs during OAE 2, the average rates at
384 stages C4 and C5 relative to C3 are denoted by the ratio (C4+C5)/C3. Our
385 compilation suggests that anoxic-euxinic sites (constituting ~58% of the studied
386 locations) exhibit an average (C4+C5)/C3 ratio of 2.39 for OC MARs. Suboxic-
387 anoxic sites (constituting ~30% of all sites) display a mean (C4+C5)/C3 ratio of 1.29.

The remaining ~12% of sites, categorized as oxic-suboxic, demonstrate a mean (C4+C5)/C3 ratio of 0.89 (Fig. 7; Table 2). A trend toward more reducing conditions during stages C4 and C5 of OAE 2 is indicated by high accumulation rates of redox-sensitive elements (Kolonic et al., 2005). Taken together, our analyses suggest that oxygen availability played an important role in controlling organic carbon burial during OAE 2. For sites deposited in shallow well-oxygenated water (including the Qiangdong section) organic matter was nearly completely oxidized prior to burial. By contrast, anoxic to euxinic conditions would have diminished organic carbon remineralization rates and promoted organic carbon preservation and burial (e.g., Takashima et al., 2011; Westermann et al., 2014).

Our compilation confirms the correlation between OC MARs and redox conditions, but there is clear overlap in OC MAR values between different redox states (Table 1). This overlap can partly be attributed to the broad and overlapping redox classifications utilized. Moreover, diverse proxies employed for inferring OAE 2 redox vary in their efficacy and interpretation (e.g., Algeo and Liu, 2020). Different redox indicators may represent conditions in different parts of the sediment/water column (e.g., Hetzel et al., 2009). Additionally, redox interpretations can be equivocal, for example, black shales in the Tethyan Himalayas marked by low bioturbation but also low TOC content (Wang et al., 2001).

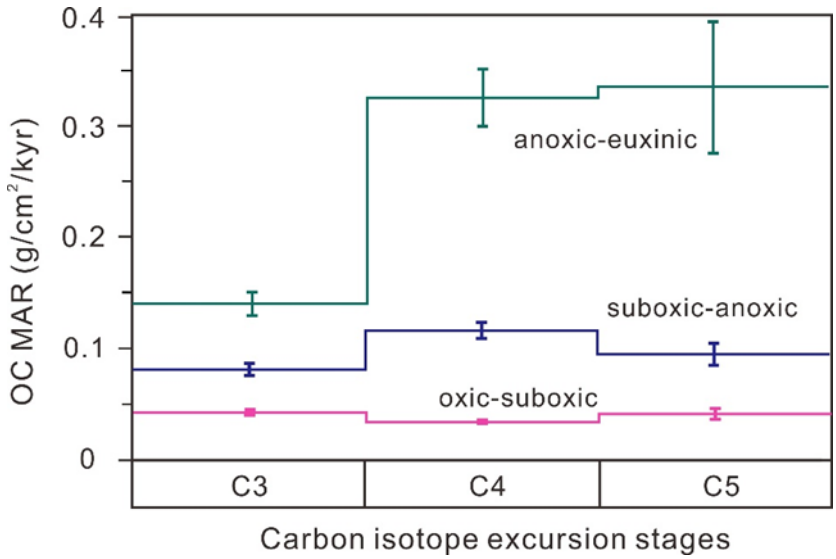

Fig. 7. Composite mean organic carbon burial rates (OC MAR) and associated 1σ uncertainties for sites with different redox environments (anoxic-euxinic, suboxic-anoxic, oxic-suboxic) in each stage of the OAE 2 CIE (stages C3-C5) obtained by bootstrap resampling, based on global compilation of all 43 sections. Detailed data are shown in Table 2.

Table 2. Data on mean organic carbon burial rates in each stage of OAE 2, obtained by bootstrap resampling. See also Fig. 5 and 7, and main text for details.

Redox condition	Number of sites (n)	Stage C3		Stage C4		Stage C5	
		mean	1 σ	mean	1 σ	mean	1 σ
Oxic-suboxic	5	0.042	0.002	0.034	0.001	0.041	0.005
Suboxic-anoxic	14	0.081	0.005	0.115	0.007	0.094	0.010
Anoxic-euxinic	24	0.139	0.011	0.327	0.026	0.337	0.062
Total sites	43	0.109	0.006	0.224	0.013	0.215	0.032

4.2 The role of nutrients and productivity

Previous studies have suggested that enhanced organic carbon sequestration at the onset of OAE 2 was likely initiated due to enhanced nutrient input sourced via Large Igneous Province emplacement (Du Vivier et al., 2014; Papadomanolaki et al., 2022), increased continental weathering and runoff (Blättler et al., 2011; Pogge von Strandmann et al., 2013; Van Helmond et al., 2015; Chen et al., 2021), and/or via

hydrothermal alteration of basalts (Trabucho Alexandre et al., 2010). Benthic regeneration of nutrients could also have significantly contributed to sustaining primary productivity (e.g., Kuypers et al., 2002; Mort et al., 2008; Beil et al., 2020).

Phosphorus is the primary limiting nutrient controlling marine biological productivity on geological timescales (e.g., Rimmer et al., 2004; Paytan and McLaughlin, 2007; Schoepfer et al., 2015), and as such has the potential to mediate the occurrence of high-productivity events (e.g., Kuypers et al., 2002; Handoh and Lenton, 2003). The atomic C_{org}:P_{tot} ratio provides a proxy to assess seafloor oxygen content and the corresponding phosphorus retention ability of sediments (Algeo and Ingall, 2007; Kraal et al., 2010). Burial of phosphorus bound to iron oxides directly correlates with the mean oxygen concentration in the deep ocean (Komar and Zeebe, 2017). This means that less P is buried through P_{Fe} (i.e., more is regenerated) with decreasing oxygen levels, and P cannot be buried effectively in fully anoxic waters (Tsandev and Slomp, 2009; Komar and Zeebe, 2017). P remobilized from sediments would increase nutrient availability in the surface ocean, which in turn can promote intensified primary production and hence more oxygen consumption via organic matter respiration, thus creating a positive feedback loop.

In the Qiangdong section, C_{org}:P_{tot} ratios are significantly lower than the Redfield ratio (106:1; Redfield et al., 1963) and other productivity proxies (e.g., Ba, Ni and Cu) are not enriched (Fig. 3), indicating oligotrophic conditions. The sediments in the Qiangdong section were deposited in a well-oxygenated shallow marine environment, where P remobilization was clearly limited. Limited nutrient input could be

444 responsible for the low OC MAR observed at Qiangdong and other oxic sites in the
445 compilation. In oxygenated shallow marine systems, phosphorus availability is
446 predominantly regulated by terrestrial fluxes and is directly utilized to sustain primary
447 productivity (Ruttenberg, 2003). As noted earlier, OC MAR in Qiangdong is slightly
448 higher in stage C3 than that observed in stages C4 and C5. This phenomenon could be
449 because of higher nutrient fluxes from the continents due to enhanced weathering
450 intensity during C3, as evidenced by zinc and lithium isotope data (e.g., Pogge von
451 Strandmann et al., 2013; Chen et al., 2021).

452 For all 43 compiled sites, C_{org}:P_{tot} ratio data are available from 11 sections,
453 covering diverse redox conditions. These data are from our Qiangdong section (oxic-
454 suboxic), the North Atlantic (anoxic-euxinic) and WIS (suboxic-anoxic). A robust
455 correlation between C_{org}:P_{tot} ratios and OC MAR at these sites is observed (Fig. 8).
456 Therefore, at the sites where anoxic to euxinic conditions prevailed during OAE 2,
457 high OC MAR in stages C4 and C5 likely resulted from the positive feedback loop of
458 remobilization of phosphorus, which stimulated productivity and further facilitated
459 anoxia. At sites characterized by relatively oxic conditions, there is no positive
460 feedback mechanism for phosphorus, resulting in low C_{org}:P_{tot} ratio and diminished
461 organic matter burial.

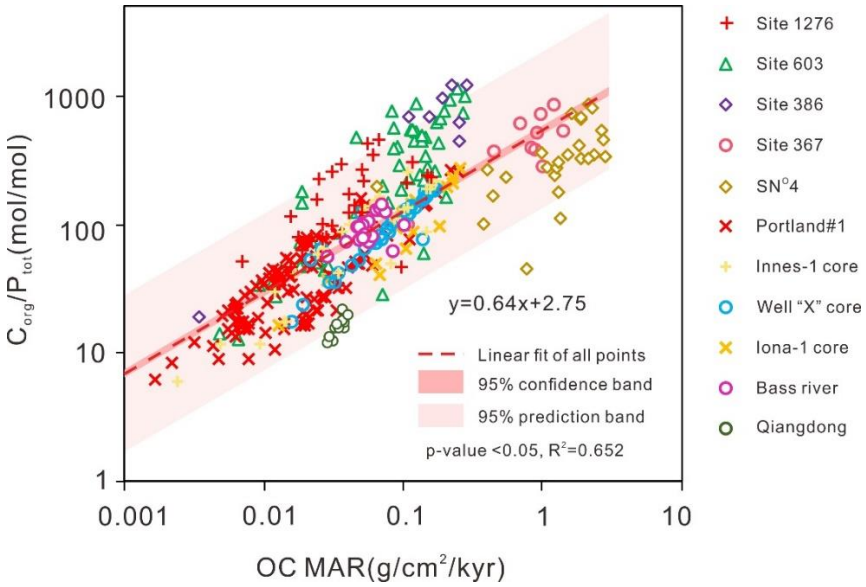

Fig. 8. Cross plot of OC MAR (g/cm^2/kyr) and C_{org}/P_{tot} (mol/mol) from 11 sites where the C_{org}:P_{tot} ratio data are available showing a significant positive correlation ($R^2 = 0.652$, P-value <0.05). The data sources for each point are shown in Table 1.

4.3 Quantifying nutrient influx during OAE 2

Enhanced nutrient influx and productivity has long been regarded as a probable trigger for OAEs generally and increased OC MAR (e.g., Jenkyns, 2003). However, the magnitude of nutrient input changes required through this mechanism is not well constrained quantitively. In this study, we modelled the inferred OC MAR changes during OAE 2 using the SCION model (Fig. 9). The seawater P reservoir size (Fig. 9A) was influenced by an artificial riverine nutrient P input forcing (or by altering P fluxes from sediment remobilization), to match the OC MAR records. When phosphorus inputs are set to rise in a two-stage pattern across stages C3 and C4 (Fig. 9A), the model yields an OC MAR curve that best fits with our empirically determined composite curve (Fig. 9B). To reproduce the maximum empirically determined OC MAR values in C4 and C5, a ~140% (i.e. 2.4-fold) increase in P concentration is

required relative to background values. The increase in OC MAR in stage C3 requires a more modest increase in P availability (~30% increase). In this scenario, the model also indicates a two-stage increase in primary productivity, ocean anoxia (quantified as an area percentage of anoxic seafloor) and a corresponding increase in the proportion of organic carbon buried (Fig. 9C, D and F). In detail, productivity during stages C4 and C5 underwent a 40% increase compared to stage C3 (Fig. 9C). Meanwhile, the increase in the modelled area of anoxic seafloor undergoes only a slight increase across the start of OAE 2 in C3. However, the modelled area of anoxic seafloor increases substantially in stages C4 and C5, and is ~24 times larger in stages C4 and C5 (~12%) compared to stage C3 (~0.5%) (Fig. 9D). This is consistent with previous work, corroborating the magnitude of oceanic anoxia expansion during stages C4 and C5 provided by previous geochemical studies using global redox proxies (e.g., sulfur isotope and uranium isotope) (Owens et al., 2013; Clarkson et al., 2018). These results indicate that intensified ocean anoxia coupled with enhanced productivity synergistically contributed to the elevated organic carbon burial observed in the stages C4 and C5, corroborating our findings discussed in Sections 4.1 and 4.2. The magnitude of the output $\delta^{13}C_{org}$ (~4–6‰) in our model is slightly higher than that observed in geological data (~3‰) (Papadomanolaki et al., 2022; Fig. 9E), with the shape also slightly differing from the geological record (Li et al., 2017). A possible explanation for the larger modelled CIE amplitude could be the missing consideration of isotopically lighter carbon input, mainly from the LIP magmatisms and enhanced carbonate burial during the OAE 2, which would reduce the proportion of organic

carbon output and the corresponding carbon isotope values. In addition, simply comparing the modelled marine organic carbon burial fluxes to the OC MAR record may lead to underestimate the varying degrees of loss of organic carbon after deposition. The model outputs are simply compared to the average record of OC MAR, which simplified our modelling strategy but neglected the possible existence of extremely high/low carbon burial in some intervals and could result in the mismatched $\delta^{13}C$ morphologies.

Our modelling results show that lower OC MAR in stage C3 compared to stages C4 and C5 could have resulted from a lower P reservoir size and lower productivity (Fig. 9A and C). It is noteworthy, however, that only the global average state of each CIE stage is modelled. Therefore, it is possible that some locally lower OC MAR in stage C3 than in stages C4 and C5 could have resulted from the reoxygenation of benthic water in the proto-Atlantic region during the upper part of stage C3, i.e. in the Plenus Cold Event (O'Connor et al., 2020).

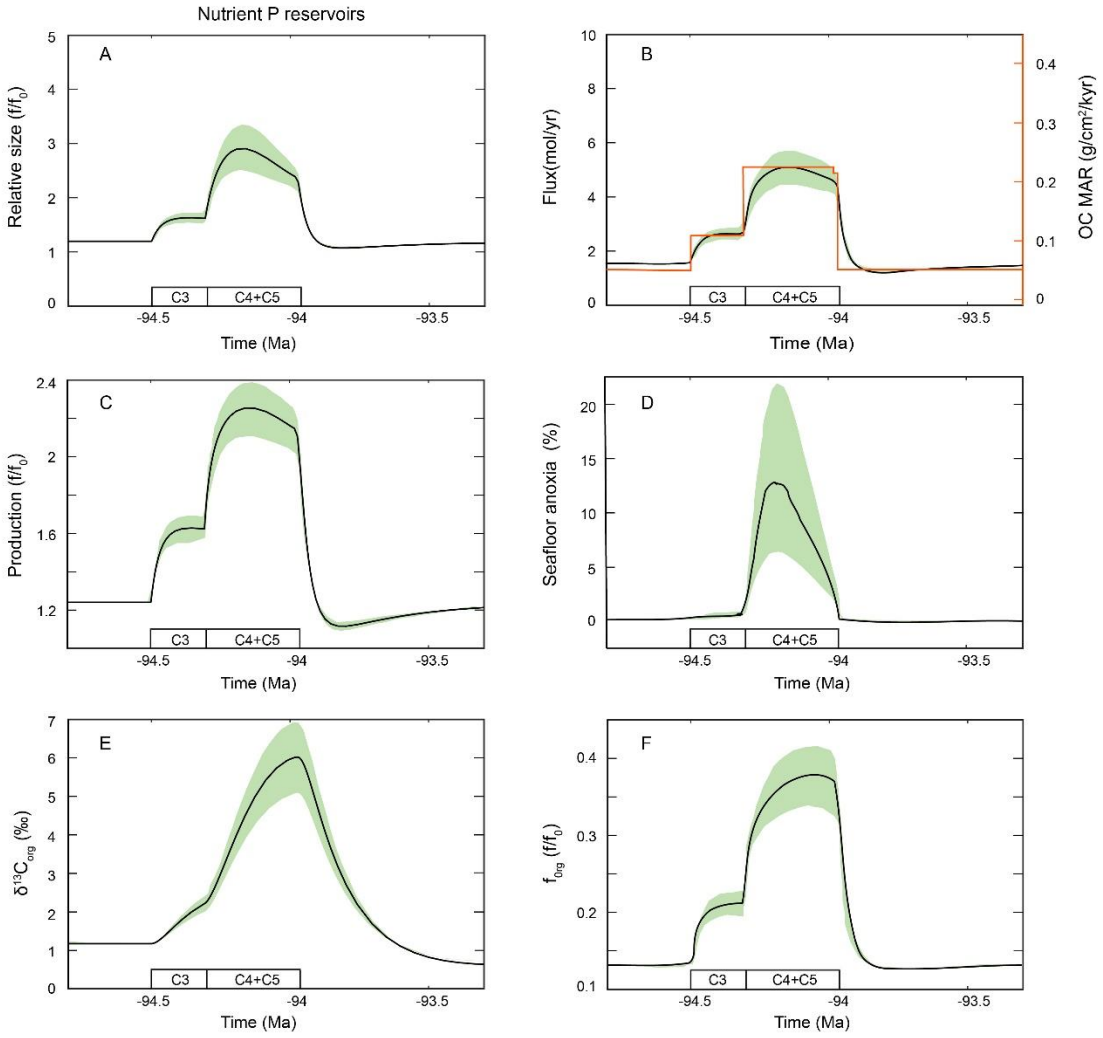

Fig. 9. SCION model outputs under a varying P input. The age model (horizontal axis) is estimated by assuming the durations of each phase and the starting age of the stage C3 at ~94.5 Ma. (A) Modelled ocean nutrient P reservoir size relative to modern level (f/f_0); (B) Modelled organic carbon burial rates (black line) and empirically determined OC MAR from our compilation (red line) (also shown in Fig. 4); (C) Modelled primary productivity relative to modern level (f/f_0); (D) Modelled seafloor anoxia (%); (E) $\delta^{13}C_{org}$ (‰); (F) Percentage of organic carbon in total carbon burial. Shaded green areas are the 20% uncertainties in the artificial P input and its effects on the modelling results.

Conclusions

In this study, we present new organic carbon isotope ($\delta^{13}C$), total organic carbon

(TOC) and trace element concentrations from the Qiangdong section in southern Tibet, China. The absence of redox-sensitive trace element (RSTE) enrichments in this section suggests prevailing oxic conditions and relatively low productivity. Our analysis of this site and a global compilation of OAE 2 sites shows that anoxic-euxinic environments were associated with the most significant increases in organic carbon burial. Our study underscores the major influence of redox conditions on organic enrichment and burial rates. An observed positive correlation between C_{org}:P_{tot} ratios and OC MARs from our compiled sites suggests enhanced anoxia during stages C4 and C5 of OAE 2. Anoxia was likely driven and promoted by a positive feedback loop owing to increased remobilization of P from anoxic-euxinic sediments, which then further promoted and sustained productivity and oxygen consumption in the water column. Conversely, well-oxygenated environments lacked this feedback, leading to lower organic carbon burial rates in stages C4 and C5. Model simulations that reconstruct the observed OC MAR trends in our compiled data suggest that productivity during stages C4 and C5 underwent a 40% increase compared to stage C3, and that areal extent of anoxic seafloor during OAE 2 in stages C4 and C5 was approximately 24 times larger than in stage C3.

Acknowledgements

This work is financially supported by the National Natural Science Foundation of China (42050102), National Key R&D Program of China (2023YFF0804000) and Fundamental Research Funds for the Central Universities (2652023001). It

contributes to IGCP 739.

References

Algeo, T.J., Ingall, E., 2007. Sedimentary Corg: P ratios, paleocean ventilation, and Phanerozoic atmospheric pO2. Palaeogeography, Palaeoclimatology, Palaeoecology 256, 130-155. https://doi.org/10.1016/j.palaeo.2007.02.029

Algeo, T.J., Liu, J., 2020. A re-assessment of elemental proxies for paleoredox analysis. Chemical Geology 540, 119549. https://doi.org/10.1016/j.chemgeo.2020.119549

Algeo, T.J., Maynard, J.B., 2004. Trace-element behavior and redox facies in core shales of Upper Pennsylvanian Kansas-type cyclothems. Chemical geology 206, 289-318. https://doi.org/10.1016/j.chemgeo.2003.12.009

Algeo, T.J., Tribovillard, N., 2009. Environmental analysis of paleoceanographic systems based on molybdenum–uranium covariation. Chemical Geology 268, 211-225. https://doi.org/10.1016/j.chemgeo.2009.09.001

Beil, S., Kuhnt, W., Holbourn, A., Scholz, F., Oxmann, J., Wallmann, K., Lorenzen, J., Aquit, M., Chellai, E.H., 2020. Cretaceous oceanic anoxic events prolonged by phosphorus cycle feedbacks. Climate of the Past 16, 757-782. https://doi.org/10.5194/cp-16-757-2020

Beil, S., Kuhnt, W., Holbourn, A.E., Aquit, M., Flögel, S., Chellai, E.H., Jabour, H., 2018. New insights into Cenomanian paleoceanography and climate evolution from the Tarfaya Basin, southern Morocco. Cretaceous Research 84, 451-473. https://doi.org/10.1016/j.cretres.2017.11.006

Blättler, C.L., Jenkyns, H.C., Reynard, L.M., Henderson, G.M., 2011. Significant increases in global weathering during Oceanic Anoxic Events 1a and 2 indicated by calcium isotopes. Earth and Planetary Science Letters 309, 77-88. https://doi.org/10.1016/j.epsl.2011.06.029

Bowman, A.R., Bralower, T.J., 2005. Paleoceanographic significance of high-resolution carbon isotope records across the Cenomanian–Turonian boundary in the Western Interior and New Jersey coastal plain, USA. Marine Geology 217, 305-321. https://doi.org/10.1016/j.margeo.2005.02.010

Brumsack, H.-J., 2006. The trace metal content of recent organic carbon-rich sediments: implications for Cretaceous black shale formation. Palaeogeography, Palaeoclimatology, Palaeoecology 232, 344-361. https://doi.org/10.1016/j.palaeo.2005.05.011

Bryant, R., Leckie, R.M., Bralower, T.J., Jones, M.M., Sageman, B.B., 2021. Microfossil and geochemical records reveal high-productivity paleoenvironments in the Cretaceous Western Interior Seaway during Oceanic Anoxic Event 2. Palaeogeography, Palaeoclimatology, Palaeoecology 584, 110679. https://doi.org/10.1016/j.palaeo.2021.110679

Charbonnier, G., Boulila, S., Spangenberg, J.E., Adatte, T., Föllmi, K.B., Laskar, J., 2018. Obliquity pacing of the hydrological cycle during the Oceanic Anoxic Event 2. Earth and Planetary Science Letters 499, 266-277. https://doi.org/10.1016/j.epsl.2018.07.029

Chen, X., Sageman, B.B., Yao, H., Han, K., Zou, Y., Wang, C., 2021. Zinc isotope evidence for paleoenvironmental changes during Cretaceous Oceanic Anoxic Event 2. Geology 49, 412-416. https://doi.org/10.1130/G48198.1

Clarkson, M.O., Stirling, C.H., Jenkyns, H.C., Dickson, A.J., Porcelli, D., Moy, C.M., Pogge von Strandmann, P.A.E., Cooke, I.R., Lenton, T.M., 2018. Uranium isotope evidence for two episodes

of deoxygenation during Oceanic Anoxic Event 2. Proceedings of the National Academy of Sciences 115, 2918-2923. https://doi.org/10.1073/pnas.1715278115

Danzelle, J., Riquier, L., Baudin, F., Thomazo, C., Pucéat, E., 2018. Oscillating redox conditions in the Vocontian Basin (SE France) during Oceanic Anoxic Event 2 (OAE 2). Chemical Geology 493, 136-152. https://doi.org/10.1016/j.chemgeo.2018.05.039

Danzelle, J., Riquier, L., Baudin, F., Thomazo, C., Pucéat, E., 2020. Nitrogen and carbon cycle perturbations through the Cenomanian-Turonian oceanic anoxic event 2 (~94 Ma) in the Vocontian Basin (SE France), Palaeogeography, Palaeoclimatology, Palaeoecology 538, 109443. https://doi.org/10.1016/j.palaeo.2019.109443

Dickson, A.J., Jenkyns, H.C., Porcelli, D., van den Boorn, S., Idiz, E., 2016. Basin-scale controls on the molybdenum-isotope composition of seawater during Oceanic Anoxic Event 2 (Late Cretaceous). Geochimica et Cosmochimica Acta 178, 291-306. https://doi.org/10.1016/j.gca.2015.12.036

Dickson, A.J., Saker-Clark, M., Jenkyns, H.C., Bottini, C., Erba, E., Russo, F., Gorbanenko, O., Naafs, B.D., Pancost, R.D., Robinson, S.A., 2017. A Southern Hemisphere record of global trace-metal drawdown and orbital modulation of organic-matter burial across the Cenomanian–Turonian boundary (Ocean Drilling Program Site 1138, Kerguelen Plateau). Sedimentology 64, 186-203. https://doi.org/10.1111/sed.12303

Du Vivier, A., Selby, D., Condon, D., Takashima, R., Nishi, H., 2015. Pacific 187Os/188Os isotope chemistry and U–Pb geochronology: Synchroneity of global Os isotope change across OAE 2. Earth and Planetary Science Letters 428, 204-216. https://doi.org/10.1016/j.epsl.2015.07.020

Du Vivier, A.D., Selby, D., Sageman, B.B., Jarvis, I., Gröcke, D.R., Voigt, S., 2014. Marine 187Os/188Os isotope stratigraphy reveals the interaction of volcanism and ocean circulation during Oceanic Anoxic Event 2. Earth and Planetary Science Letters 389, 23-33. https://doi.org/10.1016/j.epsl.2013.12.024

Eldrett, J.S., Dodsworth, P., Bergman, S.C., Wright, M., Minisini, D., 2017. Water-mass evolution in the Cretaceous Western Interior Seaway of North America and equatorial Atlantic. Climate of the Past 13, 855-878. https://doi.org/10.5194/cp-13-855-2017

Eldrett, J.S., Ma, C., Bergman, S.C., Lutz, B., Gregory, F.J., Dodsworth, P., Phipps, M., Hardas, P., Minisini, D., Ozkan, A., 2015. An astronomically calibrated stratigraphy of the Cenomanian, Turonian and earliest Coniacian from the Cretaceous Western Interior Seaway, USA: Implications for global chronostratigraphy. Cretaceous Research 56, 316-344. https://doi.org/10.1016/j.cretres.2015.04.010

Erbacher, J., Friedrich, O., Wilson, P.A., Birch, H., Mutterlose, J., 2005. Stable organic carbon isotope stratigraphy across Oceanic Anoxic Event 2 of Demerara Rise, western tropical Atlantic. Geochemistry, Geophysics, Geosystems 6, Q06010. https://doi.org/10.1029/2004GC000850

Forster, A., Schouten, S., Moriya, K., Wilson, P.A., Sinninghe Damsté, J.S., 2007. Tropical warming and intermittent cooling during the Cenomanian/Turonian oceanic anoxic event 2: Sea surface temperature records from the equatorial Atlantic. Paleoceanography 22, PA1219. https://doi.org/10.1029/2006PA001349

Gale, A.S., Jenkyns, H.C., Harilaos, T., van Breugel, Y., Sinninghe Damsté, J.S., Bottini, C., Erba, E., Russo, F., Falzoni, F., Petrizzo, M.R., 2019. High-resolution bio-and chemostratigraphy of an expanded record of Oceanic Anoxic Event 2 (late Cenomanian–early Turonian) at Clot Chevalier, near Barrême, SE France (Vocontian Basin). Newsletters on Stratigraphy 52, 97-129. https://dx.doi.org/10.1127/nos/2018/0445

Gambacorta, G., Bersezio, R., Weissert, H., Erba, E., 2016. Onset and demise of Cretaceous oceanic anoxic events: The coupling of surface and bottom oceanic processes in two pelagic basins of the western Tethys. Paleoceanography 31, 732-757. https://doi.org/10.1002/2015PA002922

Gangl, S.K., Moy, C.M., Stirling, C.H., Jenkyns, H.C., Crampton, J.S., Clarkson, M.O., Ohneiser, C., Porcelli, D., 2019. High-resolution records of Oceanic Anoxic Event 2: Insights into the timing, duration and extent of environmental perturbations from the palaeo-South Pacific Ocean. Earth and Planetary Science Letters 518, 172-182. https://doi.org/10.1016/j.epsl.2019.04.028

Goddéris, Y., Donnadieu, Y., Le Hir, G., Lefebvre, V., Nardin, E., 2014. The role of palaeogeography in the Phanerozoic history of atmospheric CO2 and climate. Earth-Science Reviews 128, 122-138. https://doi.org/10.1016/j.earscirev.2013.11.004

Handoh, I.C., Lenton, T.M., 2003. Periodic mid-Cretaceous oceanic anoxic events linked by oscillations of the phosphorus and oxygen biogeochemical cycles. Global Biogeochemical Cycles 17, 1092. https://doi.org/10.1029/2003GB002039

Haq, B.U., 2014. Cretaceous eustasy revisited. Global and Planetary change 113, 44-58. https://doi.org/10.1016/j.gloplacha.2013.12.007

Hetzel, A., Böttcher, M.E., Wortmann, U.G., Brumsack, H.-J., 2009. Paleo-redox conditions during OAE 2 reflected in Demerara Rise sediment geochemistry (ODP Leg 207). Palaeogeography, Palaeoclimatology, Palaeoecology 273, 302-328. https://doi.org/10.1016/j.palaeo.2008.11.005

Herrle, J.O., Schröder-Adams, C.J., Davis, W., Pugh, A.T., Galloway, J.M., Fath, J., 2015. Mid-Cretaceous High Arctic stratigraphy, climate, and Oceanic Anoxic Events. Geology 43, 403-406. https://doi.org/10.1130/G36439.1

Jarvis, I., Gale, A.S., Jenkyns, H.C., Pearce, M.A., 2006. Secular variation in Late Cretaceous carbon isotopes: a new δ13C carbonate reference curve for the Cenomanian–Campanian (99.6–70.6 Ma). Geological Magazine 143, 561-608. https://doi.org/10.1017/S0016756806002421

Jarvis, I., Lignum, J.S., Gröcke, D.R., Jenkyns, H.C., Pearce, M.A., 2011. Black shale deposition, atmospheric CO2drawdown, and cooling during the Cenomanian-Turonian Oceanic Anoxic Event. Paleoceanography 26, PA3201. https://doi.org/10.1029/2010PA002081

Jenkyns, H., 1980. Cretaceous anoxic events: from continents to oceans. Journal of the Geological Society 137, 171-188. https://doi.org/10.1144/gsjgs.137.2.0171

Jenkyns, H.C., 2003. Evidence for rapid climate change in the Mesozoic–Palaeogene greenhouse world. Philosophical Transactions of the Royal Society of London. Series A: Mathematical, Physical and Engineering Sciences 361, 1885-1916. https://doi.org/10.1098/rsta.2003.1240

Jenkyns, H.C., 2010. Geochemistry of oceanic anoxic events. Geochemistry, Geophysics, Geosystems 11, Q03004. https://doi.org/10.1029/2009GC002788

Jenkyns, H.C., Dickson, A.J., Ruhl, M., Van den Boorn, S.H., 2017. Basalt-seawater interaction, the Plenus Cold Event, enhanced weathering and geochemical change: deconstructing Oceanic Anoxic Event 2 (Cenomanian–Turonian, Late Cretaceous). Sedimentology 64, 16-43. https://doi.org/10.1111/sed.12305

Jia, J., Wan, X., Li, G., Chen, H., 2010. Benthic foraminifera as paleoenvironmental indicators and their paleoceanographic significance around the Cenomanian-Turonian boundary in Gamba, Tibet. Acta Micropaleotonlogica Sinica 27, 135-143.

Jones, M.M., Sageman, B.B., Oakes, R.L., Parker, A.L., Leckie, R.M., Bralower, T.J., Sepúlveda, J., Fortiz, V., 2019. Astronomical pacing of relative sea level during Oceanic Anoxic Event 2: Preliminary studies of the expanded SH#1 Core, Utah, USA. GSA Bulletin 131, 1702-1722.

https://doi.org/10.1130/B32057.1
Jones, M.M., Sageman, B.B., Selby, D., Jicha, B.R., Singer, B.S., Titus, A.L., 2021. Regional chronostratigraphic synthesis of the Cenomanian-Turonian oceanic anoxic event 2 (OAE2) interval, Western Interior Basin (USA): New Re-Os chemostratigraphy and 40Ar/39Ar geochronology. GSA Bulletin 133, 1090-1104. https://doi.org/10.1130/B35594.1
Kalanat, B., Mahmudy-Gharaie, M.H., Vahidinia, M., Vaziri-Moghaddam, H., Kano, A., Kumon, F., 2018. Paleoenvironmental perturbation across the Cenomanian/Turonian boundary of the Kopet-Dagh Basin (NE Iran), inferred from geochemical anomalies and benthic foraminiferal assemblages. Cretaceous Research 86, 261-275. https://doi.org/10.1016/j.cretres.2017.09.019
Kemp, D.B., Suan, G., Fantasia, A., Jin, S., Chen, W., 2022. Global organic carbon burial during the Toarcian oceanic anoxic event: Patterns and controls. Earth-Science Reviews 231, 104086. https://doi.org/10.1016/j.earscirev.2022.104086
Kolonic, S., Wagner, T., Forster, A., Sinninghe Damsté, J.S., Walsworth-Bell, B., Erba, E., Turgeon, S., Brumsack, H.J., Chellai, E.H., Tsikos, H., 2005. Black shale deposition on the northwest African Shelf during the Cenomanian/Turonian oceanic anoxic event: Climate coupling and global organic carbon burial. Paleoceanography 20, PA1006. https://doi.org/10.1029/2003PA000950
Komar, N., Zeebe, R.E., 2017. Redox-controlled carbon and phosphorus burial: A mechanism for enhanced organic carbon sequestration during the PETM. Earth and Planetary Science Letters 479, 71-82. https://doi.org/10.1016/j.epsl.2017.09.011
Kraal, P., Slomp, C.P., Forster, A., Kuypers, M.M.M., 2010. Phosphorus cycling from the margin to abyssal depths in the proto-Atlantic during oceanic anoxic event 2. Palaeogeography, Palaeoclimatology, Palaeoecology 295, 42-54. https://doi.org/10.1016/j.palaeo.2010.05.014
Kump, L.R., 1991. Interpreting carbon-isotope excursions: Strangelove oceans. Geology 19, 299-302. https://doi.org/10.1130/0091-7613(1991)019<0299:ICIESO>2.3.CO;2
Kuypers, M.M., Pancost, R.D., Nijenhuis, I.A., Sinninghe Damsté, J.S., 2002. Enhanced productivity led to increased organic carbon burial in the euxinic North Atlantic basin during the late Cenomanian oceanic anoxic event. Paleoceanography 17, 1051. https://doi.org/10.1029/2000PA000569
Lenniger, M., Nøhr-Hansen, H., Hills, L.V., Bjerrum, C.J., 2014. Arctic black shale formation during Cretaceous Oceanic Anoxic Event 2. Geology 42, 799-802. https://doi.org/10.1130/G35732.1
Li, X., Jenkyns, H.C., Wang, C., Hu, X., Chen, X., Wei, Y., Huang, Y., Cui, J., 2006. Upper Cretaceous carbon-and oxygen-isotope stratigraphy of hemipelagic carbonate facies from southern Tibet, China. Journal of the Geological Society 163, 375-382. https://doi.org/10.1144/0016-764905-046
Li, Y.-X., Montanez, I.P., Liu, Z., Ma, L., 2017. Astronomical constraints on global carbon-cycle perturbation during Oceanic Anoxic Event 2 (OAE2). Earth and Planetary Science Letters 462, 35-46. https://doi.org/10.1016/j.epsl.2017.01.007
Londoño, V., Collins, L.S., 2022. Controls on sedimentary accumulation of organic matter during Cretaceous Oceanic Anoxic Event 2, IODP site U1407, Southeast Newfoundland Ridge. Marine Geology 443, 106699. https://doi.org/10.1016/j.margeo.2021.106699
Lowery, C.M., Cunningham, R., Barrie, C.D., Bralower, T., Snedden, J.W., 2017. The Northern Gulf of Mexico During OAE2 and the Relationship Between Water Depth and Black Shale Development. Paleoceanography 32, 1316-1335. https://doi.org/10.1002/2017PA003180
Lowery, C.M., Self-Trail, J.M., Barrie, C.D., 2021. Enhanced terrestrial runoff during Oceanic Anoxic Event 2 on the North Carolina Coastal Plain, USA. Climate of the Past 17, 1227-1242.

https://doi.org/10.5194/cp-17-1227-2021
Ma, C., Meyers, S.R., Sageman, B.B., Singer, B.S., Jicha, B.R., 2014. Testing the astronomical time scale for oceanic anoxic event 2, and its extension into Cenomanian strata of the Western Interior Basin (USA). GSA Bulletin 126, 974-989. https://doi.org/10.1130/B30922.1
McDonald, B.S., Partin, C.A., Sageman, B., Holmden, C., 2022. Uranium isotope reconstruction of ocean deoxygenation during OAE 2 hampered by uncertainties in fractionation factors and local U-cycling. Geochimica et Cosmochimica Acta 331, 143-164. https://doi.org/10.1016/j.gca.2022.05.010
Meyers, S.R., Siewert, S.E., Singer, B.S., Sageman, B.B., Condon, D.J., Obradovich, J.D., Jicha, B.R., Sawyer, D.A., 2012. Intercalibration of radioisotopic and astrochronologic time scales for the Cenomanian-Turonian boundary interval, Western Interior Basin, USA. Geology 40, 7-10. https://doi.org/10.1130/G32261.1
Mills, B.J., Donnadieu, Y., Goddéris, Y., 2021. Spatial continuous integration of Phanerozoic global biogeochemistry and climate. Gondwana Research 100, 73-86. https://doi.org/10.1016/j.gr.2021.02.011
Monteiro, F.M., Pancost, R.D., Ridgwell, A., Donnadieu, Y., 2012. Nutrients as the dominant control on the spread of anoxia and euxinia across the Cenomanian-Turonian oceanic anoxic event (OAE2): Model-data comparison. Paleoceanography 27, PA4209. https://doi.org/10.1029/2012PA002351
Mort, H.P., Adatte, T., Keller, G., Bartels, D., Föllmi, K.B., Steinmann, P., Berner, Z., Chellai, E., 2008. Organic carbon deposition and phosphorus accumulation during Oceanic Anoxic Event 2 in Tarfaya, Morocco. Cretaceous Research 29, 1008-1023. https://doi.org/10.1016/j.cretres.2008.05.026
O'Connor, L.K., Jenkyns, H.C., Robinson, S.A., Remmelzwaal, S.R.C., Batenburg, S.J., Parkinson, I.J., Gale, A.S., 2020. A Re-evaluation of the Plenus Cold Event, and the Links Between CO2, Temperature, and Seawater Chemistry During OAE 2. Paleoceanography and Paleoclimatology 35, e2019PA003631. https://doi.org/10.1029/2019PA003631
Owens, J.D., Gill, B.C., Jenkyns, H.C., Bates, S.M., Severmann, S., Kuypers, M.M., Woodfine, R.G., Lyons, T.W., 2013. Sulfur isotopes track the global extent and dynamics of euxinia during Cretaceous Oceanic Anoxic Event 2. Proceedings of the National Academy of Sciences 110, 18407-18412. https://doi.org/10.1073/pnas.1305304110
Owens, J.D., Lyons, T.W., Hardisty, D.S., Lowery, C.M., Lu, Z., Lee, B., Jenkyns, H.C., 2017. Patterns of local and global redox variability during the Cenomanian–Turonian Boundary Event (Oceanic Anoxic Event 2) recorded in carbonates and shales from central Italy. Sedimentology 64, 168-185. https://doi.org/10.1111/sed.12352
Owens, J.D., Lyons, T.W., Lowery, C.M., 2018. Quantifying the missing sink for global organic carbon burial during a Cretaceous oceanic anoxic event. Earth and Planetary Science Letters 499, 83-94. https://doi.org/10.1016/j.epsl.2018.07.021
Paez-Reyes, M., Carvajal-Ortiz, H., Sahoo, S.K., Varol, O., Miller, B.V., Hughes, G.W., Gaona-Narvaez, T., Patarroyo, G.D., Curtis, J.H., Lerma, I., Copeland, P., 2021. Assessing the contribution of the La Luna Sea to the global sink of organic carbon during the Cenomanian-Turonian Oceanic Anoxic Event 2 (OAE2). Global and Planetary Change 199, 103424. https://doi.org/10.1016/j.gloplacha.2021.103424
Papadomanolaki, N.M., van Helmond, N.A.G.M., Pälike, H., Sluijs, A., Slomp, C.P., 2022. Quantifying volcanism and organic carbon burial across Oceanic Anoxic Event 2. Geology 50, 511-515.

https://doi.org/10.1130/G49649.1
Paytan, A., McLaughlin, K., 2007. The oceanic phosphorus cycle. Chemical reviews 107, 563-576. https://doi.org/10.1021/cr0503613
Pogge von Strandmann, P.A., Jenkyns, H.C., Woodfine, R.G., 2013. Lithium isotope evidence for enhanced weathering during Oceanic Anoxic Event 2. Nature Geoscience 6, 668-672. https://doi.org/10.1038/ngeo1875
Poulton, S.W., Henkel, S., März, C., Urquhart, H., Flögel, S., Kasten, S., Sinninghe Damsté, J.S., Wagner, T., 2015. A continental-weathering control on orbitally driven redox-nutrient cycling during Cretaceous Oceanic Anoxic Event 2. Geology 43, 963-966. https://doi.org/10.1130/G36837.1
Prokoph, 2001. Geochronology and calibration of global Milankovitch cyclicity at the Cenomanian-Turonian boundary. Geology 29, 523-526. https://doi.org/10.1130/0091-7613(2001)029<0523:GACOGM>2.0.CO;2
Redfield, A., Ketchum, B., Richards, F., 1963. The influence of organisms on the composition of seawater. The sea 2, 26-77.
Rimmer, S.M., Thompson, J.A., Goodnight, S.A., Robl, T.L., 2004. Multiple controls on the preservation of organic matter in Devonian–Mississippian marine black shales: geochemical and petrographic evidence. Palaeogeography, Palaeoclimatology, Palaeoecology 215, 125-154. https://doi.org/10.1016/j.palaeo.2004.09.001
Ruttenberg, K., 2003. The global phosphorus cycle. Treatise on geochemistry 8, 585-634. https://doi.org/10.1016/B0-08-043751-6/08153-6
Sageman, B.B., Meyers, S.R., Arthur, M.A., 2006. Orbital time scale and new C-isotope record for Cenomanian-Turonian boundary stratotype. Geology 34, 125-128. https://doi.org/10.1130/G22074.1
Schlanger, S., Arthur, M., Jenkyns, H., Scholle, P., 1987. The Cenomanian-Turonian Oceanic Anoxic Event, I. Stratigraphy and distribution of organic carbon-rich beds and the marine δ13C excursion. Geological Society, London, Special Publications 26, 371-399. https://doi.org/10.1144/GSL.SP.1987.026.01.24
Schlanger, S., Jenkyns, H., 1976. Cretaceous oceanic anoxic events: causes and consequences. Geologie en mijnbouw 55.
Schoepfer, S.D., Shen, J., Wei, H., Tyson, R.V., Ingall, E., Algeo, T.J., 2015. Total organic carbon, organic phosphorus, and biogenic barium fluxes as proxies for paleomarine productivity. Earth-Science Reviews 149, 23-52. https://doi.org/10.1016/j.earscirev.2014.08.017
Schröder-Adams, C.J., Herrle, J.O., Selby, D., Quesnel, A., Froude, G., 2019. Influence of the high arctic igneous province on the cenomanian/turonian boundary interval, sverdrup basin, high canadian arctic. Earth and Planetary Science Letters 511, 76-88. https://doi.org/10.1016/j.epsl.2019.01.023
Scotese, C.R., 2016. Tutorial: PALEOMAP paleoAtlas for GPlates and the paleoData plotter program. PALEOMAP Project, Technical Report 56. http://www.earthbyte.org/paleomap-paleoatlas-for-gplates
Sepúlveda, J., Wendler, J., Leider, A., Kuss, H.-J., Summons, R.E., Hinrichs, K.-U., 2009. Molecular isotopic evidence of environmental and ecological changes across the Cenomanian–Turonian boundary in the Levant Platform of central Jordan. Organic Geochemistry 40, 553-568. https://doi.org/10.1016/j.orggeochem.2009.02.009

Singh, K., Xie, M., 2008. Bootstrap: a statistical method. Unpublished manuscript, Rutgers University, USA. Retrieved from http://www. stat. rutgers. edu/home/mxie/RCPapers/bootstrap. pdf, 1-14.

Takashima, R., Nishi, H., Huber, B.T., Leckie, R.M., 2006. Greenhouse world and the Mesozoic ocean. Oceanography 19, 82-92.

Takashima, R., Nishi, H., Yamanaka, T., Tomosugi, T., Fernando, A.G., Tanabe, K., Moriya, K., Kawabe, F., Hayashi, K., 2011. Prevailing oxic environments in the Pacific Ocean during the mid-Cretaceous Oceanic anoxic event 2. Nature Communications 2, 234. https://doi.org/10.1038/ncomms1233

Taylor, S.R., McLennan, S.M., 1985. The continental crust: its composition and evolution.

Tessin, A., Hendy, I., Sheldon, N., Sageman, B., 2015. Redox-controlled preservation of organic matter during "OAE 3" within the Western Interior Seaway. Paleoceanography 30, 702-717. https://doi.org/10.1002/2014PA002729

Trabucho Alexandre, J., Tuenter, E., Henstra, G.A., van der Zwan, K.J., van de Wal, R.S., Dijkstra, H.A., de Boer, P.L., 2010. The mid-Cretaceous North Atlantic nutrient trap: black shales and OAEs. Paleoceanography 25, PA4201. https://doi.org/10.1029/2010PA001925

Tribovillard, N., Algeo, T., Baudin, F., Riboulleau, A., 2012. Analysis of marine environmental conditions based onmolybdenum–uranium covariation-Applications to Mesozoic paleoceanography. Chemical Geology 324, 46-58. https://doi.org/10.1016/j.chemgeo.2011.09.009

Tribovillard, N., Algeo, T.J., Lyons, T., Riboulleau, A., 2006. Trace metals as paleoredox and paleoproductivity proxies: an update. Chemical geology 232, 12-32. https://doi.org/10.1016/j.chemgeo.2006.02.012

Tsandev, I., Slomp, C., 2009. Modeling phosphorus cycling and carbon burial during Cretaceous Oceanic Anoxic Events. Earth and Planetary Science Letters 286, 71-79. https://doi.org/10.1016/j.epsl.2009.06.016

Tsikos, H., Jenkyns, H., Walsworth-Bell, B., Petrizzo, M., Forster, A., Kolonic, S., Erba, E., Silva, I.P., Baas, M., Wagner, T., 2004. Carbon-isotope stratigraphy recorded by the Cenomanian–Turonian Oceanic Anoxic Event: correlation and implications based on three key localities. Journal of the Geological Society 161, 711-719. https://doi.org/10.1144/0016-764903-077

Turgeon, S., Brumsack, H.-J., 2006. Anoxic vs dysoxic events reflected in sediment geochemistry during the Cenomanian–Turonian Boundary Event (Cretaceous) in the Umbria–Marche Basin of central Italy. Chemical Geology 234, 321-339. https://doi.org/10.1016/j.chemgeo.2006.05.008

Turgeon, S.C., Creaser, R.A., 2008. Cretaceous oceanic anoxic event 2 triggered by a massive magmatic episode. Nature 454, 323-326. https://doi.org/10.1038/nature07076

van Helmond, N.A., Sluijs, A., Reichart, G.-J., Sinninghe Damsté, J.S., Slomp, C.P., Brinkhuis, H., 2014a. A perturbed hydrological cycle during Oceanic Anoxic Event 2. Geology 42, 123-126. https://doi.org/10.1130/G34929.1

van Helmond, N.A.G.M., Ruvalcaba Baroni, I., Sluijs, A., Sinninghe Damsté, J.S., Slomp, C.P., 2014b. Spatial extent and degree of oxygen depletion in the deep proto-North Atlantic basin during Oceanic Anoxic Event 2. Geochemistry, Geophysics, Geosystems 15, 4254-4266. https://doi.org/10.1002/2014GC005528

Van Helmond, N., Sluijs, A., Sinninghe Damsté, J., Reichart, G.-J., Voigt, S., Erbacher, J., Pross, J., Brinkhuis, H., 2015. Freshwater discharge controlled deposition of Cenomanian–Turonian black shales on the NW European epicontinental shelf (Wunstorf, northern Germany). Climate of the Past 11, 495-508. https://doi.org/10.5194/cp-11-495-2015

Voigt, S., Aurag, A., Leis, F., Kaplan, U., 2007. Late Cenomanian to Middle Turonian high-resolution carbon isotope stratigraphy: New data from the Münsterland Cretaceous Basin, Germany. Earth and Planetary Science Letters 253, 196-210. https://doi.org/10.1016/j.epsl.2006.10.026

Wallmann, K., 2010. Phosphorus imbalance in the global ocean? Global Biogeochemical Cycles 24, GB4030. https://doi.org/10.1029/2009GB003643

Wan, X., Wignall, P., Zhao, W., 2003. The Cenomanian–Turonian extinction and oceanic anoxic event: evidence from southern Tibet. Palaeogeography, Palaeoclimatology, Palaeoecology 199, 283-298. https://doi.org/10.1016/S0031-0182(03)00543-1

Wang, C., Hu, X., Jansa, L., Wan, X., Tao, R., 2001. The Cenomanian–Turonian anoxic event in southern Tibet. Cretaceous Research 22, 481-490. https://doi.org/10.1006/cres.2001.0271

Wang, J., Bulot, L.G., Taylor, K.G., Redfern, J., 2021. Controls and timing of Cenomanian-Turonian organic enrichment and relationship to the OAE2 event in Morocco, North Africa. Marine and Petroleum Geology 128, 105013. https://doi.org/10.1016/j.marpetgeo.2021.105013

Westermann, S., Vance, D., Cameron, V., Archer, C., Robinson, S.A., 2014. Heterogeneous oxygenation states in the Atlantic and Tethys oceans during Oceanic Anoxic Event 2. Earth and Planetary Science Letters 404, 178-189. https://doi.org/10.1016/j.epsl.2014.07.018

Zhang, X., Chen, K., Hu, D., Sha, J., 2016. Mid-Cretaceous carbon cycle perturbations and Oceanic Anoxic Events recorded in southern Tibet. Scientific Reports 6, 39643. https://doi.org/10.1038/srep39643

Zhang, Y., Benjamin, M., He, T., Yang, T., Zhu, M., 2023. Simulating the long-term carbon cycle in the Phanerozoic: Current status and future developments. Chinese Science Bulletin 68, 1580-1592.